

---

# Beyond Known Reality: Exploiting Counterfactual Explanations for Medical Research

---

Toygar Tanyel<sup>φ,γ</sup> Serkan Ayvaz<sup>γ,μ</sup> Bilgin Keserci<sup>α,ω,\*</sup>

<sup>φ</sup>Department of Biomedical Engineering, Istanbul Technical University

<sup>γ</sup>Department of Computer Engineering, Yildiz Technical University

<sup>μ</sup>Department of Software Engineering, University of Southern Denmark

<sup>α</sup>Department of Biomedical Engineering, Yildiz Technical University

<sup>ω</sup>Intelligent Healthcare & Innovation Research Center

tanyel23@itu.edu.tr sayvaz@yildiz.edu.tr \*bushido.keserci@gmail.com

## ABSTRACT

This study employs counterfactual explanations to explore "what if?" scenarios in medical research, with the aim of expanding our understanding beyond existing boundaries. Specifically, we focus on utilizing MRI features for diagnosing pediatric posterior fossa brain tumors as a case study. The field of artificial intelligence and explainability has witnessed a growing number of studies and increasing scholarly interest. However, the lack of human-friendly interpretations in explaining the outcomes of machine learning algorithms has significantly hindered the acceptance of these methods by clinicians in their clinical practice. To address this, our approach incorporates counterfactual explanations, providing a novel way to examine alternative decision-making scenarios. These explanations offer personalized and context-specific insights, enabling the validation of predictions and clarification of variations under diverse circumstances. Importantly, our approach maintains both statistical and clinical fidelity, allowing for the examination of distinct tumor features through alternative realities. Additionally, we explore the potential use of counterfactuals for data augmentation and evaluate their feasibility as an alternative approach in medical research. The results demonstrate the promising potential of counterfactual explanations to enhance trust and acceptance of AI-driven methods in clinical settings.

**Keywords** counterfactual explanations · posterior fossa pediatric brain tumors · magnetic resonance imaging · explainable artificial intelligence

## 1 Introduction

As we incorporate automated decision-making systems into the real world, explainability and accountability questions become increasingly important [1]. In some fields, such as medicine and healthcare, ignoring or failing to address such a challenge can seriously limit the adoption of computer-based systems that rely on machine learning (ML) and computational intelligence methods for data analysis in real-world applications [2–4]. Previous research in Explainable Artificial Intelligence (XAI) has primarily focused on developing techniques to interpret decisions made by black box ML models. For instance, widely used approaches such as local interpretable model-agnostic explanations (LIME) [5] and shapley additive explanations (SHAP) [6] offer attribution-based explanations to interpret ML models. These methods can assist computer scientists and ML experts in understanding the reasoning behind the predictions made by AI models. However, end-users, including clinicians and patients, may be more interested in understanding the practical implications of the ML model's predictions in relation to themselves, rather than solely focusing on how the models arrived at their predictions. For example, patients' primary concern lies not only in obtaining information about their illness but also in seeking guidance on how to regain their health. Understanding the decision-making process of either the doctor or the ML model is of lesser importance to them.

---

\*Corresponding Author

Counterfactual explanations [7] are a form of model-agnostic interpretation technique that identifies the minimal changes needed in input features to yield a different output, aligned with a specific desired outcome. This approach holds promise in enhancing the interpretability and accountability of AI models by offering deeper insights into their decision-making processes. Our proposed approach aims to provide enhanced transparency regarding the relationship between MRI features, moving beyond generating actionable outcomes solely for individual patients. Through counterfactual explanations, previously unseen decisions within the decision space can be brought to light. Numerous questions can be explored, such as how to determine the modifications required to transform a patient's diagnosis from one tumor subtype to another. Initially, posing such a question may seem nonsensical and illogical since an individual's actual tumor type cannot be magically altered. However, considering the challenge of distinguishing these two tumor types in clinical settings, asking such a question can effectively demonstrate which features are more informative in differentiating tumor types. Counterfactual explanations enable us to identify the characteristics that distinguish two patient types with the smallest changes in features. Consequently, a deeper understanding of the interactions between MRI features and tumors can be gained; unveiling previously undisclosed outcomes that may be concealed in existing ML studies.

Furthermore, we have identified a potential contribution to clinical practice whereby a new patient with only MRI data available can have their tumor type estimated using a counterfactual approach, prior to receiving histopathological results. Since there is no prior label available for the patient, they are given an "unknown" label and the counterfactual approach is used for each tumor type, allowing estimation of the tumor type with the lowest distance and smallest change in features. While this approach shares similarities with ML, the crucial distinction lies in retaining information about the reasoning behind the estimated tumor type and its corresponding feature changes. This, in turn, can enhance our understanding and the use of AI models in clinical practice.

Last but not least, in situations where the acquisition of data is limited or not possible, various data augmentation methods have been developed to enhance the performance of ML and related applications [8–10]. However, these methods also give rise to additional issues while fulfilling their intended purpose, such as introducing biased shifts in data distribution. To address this issue, we employed counterfactuals generated from different spaces in order to balance the data by maximizing its diversity, and subsequently reported the results for different scenarios.

## 1.1 Brief Introduction to Posterior Fossa Pediatric Brain Tumors

Brain tumors represent the predominant form of cancer in children, constituting more than 25% of all cases. Specifically, the posterior fossa (PF) region comprises approximately 60-70% of these tumors and encompasses subtypes such as medulloblastoma (MB), ependymoma (EP), pilocytic astrocytoma (PA), and brainstem glioma (BG).

Clinical information obtained from radiological interpretations and histopathological analysis of tumors plays a crucial role in diagnosing, prognosing, and treating PF tumors in pediatric patients. Histopathological evaluation is essential for the initial diagnosis, providing valuable insights into patient prognosis and guiding clinical and therapeutic decisions. It serves as the established standard for differentiating between various PF tumor types. However, performing biopsies of different PF brain tumors carries significant risks of morbidity and mortality, in addition to being costly. Recent advancements in characterizing tumor subtypes using cross-sectional diagnostic imaging have shown promise in predicting differential survival rates and treatment responses. This progress holds significant potential for future treatment stratification in PF tumors. Hence, the advancement of a novel non-invasive diagnostic tool holds utmost importance in precisely classifying tumor type and grade, as well as aiding in treatment planning.

Magnetic resonance imaging (MRI) has emerged as the leading non-invasive imaging modality. It offers inherent advantages such as excellent soft-tissue contrast while avoiding the potential hazards of ionizing radiation. Conventional MRI protocols, including T1-weighted (T1W), T2-weighted (T2W), and fluid-attenuated inversion recovery (FLAIR) sequences, have shown promising results in distinguishing various PF tumor types in pediatric patients [11–29]. Furthermore, diffusion-weighted imaging (DWI) combined with apparent diffusion coefficient (ADC) mapping enables the assessment of physiological characteristics. It facilitates the differentiation of low- and high-grade tumors, as well as their distinct subtypes [30–40].

## 2 Material & Methods

### 2.1 Ethics Statement and Patient Characteristics

This prospective study (Ref: 352/NØ2-CØT dated 13 March 2020) was carried out in both Radiology and Neurosurgery departments, and was approved by the Institutional Review Board in accordance with the 1964 Helsinki declaration. Written informed consent was obtained from authorized guardians of patients prior to the MRI procedure. Our study comprised a cohort of 112 pediatric patients diagnosed with PF tumors, including 42 with MB, 25 with PA, 34 with BG,

and 11 with EP. All BG patients were confirmed based on full agreement between neuroradiologists and neurosurgeons, whereas the remaining MB, PA, and EP patients underwent either surgery or biopsy for histopathological confirmation.

## 2.2 Data Acquisition and Assessment of MRI Features

For all patients, MRI exams including T1W, T2W, FLAIR, DWI (b values: 0 and 1000) with ADC, and contrast-enhanced T1W (CE-T1) sequences with macrocyclic gadolinium-based contrast enhancement (0.1 ml/kg Gadovist, Bayer, Germany, or 0.2 ml/kg Dotarem, Guerbet, France) were collected in the supine position using a 1.5 Tesla MRI scanner (Multiva, Philips, Best, the Netherlands).

The Medical Imaging Interaction Toolkit (German Cancer Research Center, Division of Medical Image Computing, Heidelberg, Germany) was utilized for measuring the region of interest (ROI) of PF tumors and normal-appearing parenchyma and subsequently assessed the following MRI features: signal intensities (SIs) of T2, T1, FLAIR, T1CE, DWI, and ADC. Ratios between the PF tumor and parenchyma were calculated by dividing the SI of the tumor and the SI of the normal-appearing parenchyma based on T2, T1, FLAIR, T1CE, DWI, and ADC. Additionally, ADC values were quantified for both the PF tumor and parenchyma on the ADC map using the MR Diffusion tool available in Philips Intellispace Portal, version 11 (Philips, Best, The Netherlands). It is worth noting that, prior to analysis, bias field correction was applied to every image to correct for nonuniform grayscale intensities in the MRI caused by field inhomogeneities.

## 2.3 Standardization

Prior to conducting ML trainings, the dataset was subjected to a standardization process, using Python programming (version 3.9.13) with the Scikit-Learn library (version 1.0.2) module. This technique involved transforming the data to have a mean of zero and a standard deviation of one. To standardize all numerical attributes, the Scikit-Learn StandardScaler function was employed, which subtracted the mean and scaled the values to unit variance, ensuring the data was in a standardized format. To determine the standard score of a sample  $x_i$ , the following formula is used:

$$z = \frac{x_i - \mu}{\sigma}, \quad (1)$$

where,  $\mu$  represents the mean of the training samples, and  $\sigma$  represents their standard deviation.

## 2.4 Distance Calculation

When using counterfactuals as classifiers, the significant scale difference between the actual values of the MRI features in Tables 1 and 2 makes it illogical to calculate distances. To address this issue, we tackled the problem by disregarding the unchanged values indicated by ‘-’ and rescaling all available values to a standard scale before reintroducing them. Subsequently, we computed the distance using the Euclidean distance metric on the generated counterfactual values of the current factual (i.e., new patient). By aiming to minimize the distance, we seek to determine the tumor type in this manner, as it corresponds to the least dissimilarity (Table 3).

The Euclidean distance formula can be represented as following:

$$\text{Distance} = \sqrt{\sum_{i=1}^n (x_i - y_i)^2} \quad (2)$$

In the formula,  $x_i$  and  $y_i$  represent the values of the corresponding features in the current row and baseline row, respectively. The summation symbol  $\sum$  calculates the sum of the squared differences for each feature. Finally, the square root function is applied to obtain the Euclidean distance. Please note that in the formula, the  $n$  represents the number of features or columns in the dataset.

## 2.5 Statistical Analysis

The statistical analysis was conducted using the t-test from the scipy library (version 1.10.1). A two-tailed p-value of  $<0.05$  was considered statistically significant.

The analysis was performed as follows: First, the analysis involved assessing whether the counterfactuals generated by changing the tumor type from  $\mathcal{X}$  to  $\mathcal{Y}$  underwent a statistically significant change (dependent t-test). Second, it involved analyzing whether the counterfactuals generated by changing the tumor type from  $\mathcal{X}$  to  $\mathcal{Y}$  exhibited significant similarity to the original (factual) patients with tumor type  $\mathcal{Y}$  that we previously had (Welch’s t-test).

Five counterfactuals were generated for each patient transition from tumor type  $\mathcal{X}$  to  $\mathcal{Y}$ . When applying dependent and independent t-tests, the generated counterfactuals were tested in different ways. In the case of measuring how different the newly generated data is from the original data, we created more data than our original sample size. Therefore, we cannot satisfy the requirement for equal dimensions in the dependent analysis during the testing phase. To address this, we designed a different analysis approach: for each counterfactual, the data of the corresponding factual patient was considered as the initial data for testing. Subsequently, a significance test was performed on the old-new values of the five feature variables that changed the most for each counterfactual generated from this factual data.

In the case of independent analysis, all generated counterfactuals were independently tested by including all patients present in the real data for each of the three features that underwent the most significant changes. The corresponding values for these three features were tested independently.

In summary, the fundamental difference between the two tests can be considered as being patient-based and feature-based in nature.

## 2.6 Distribution Plotting

To generate individual kernel density estimation (KDE) plots for each feature, we utilized the `kdeplot` function from the Seaborn package (version 0.11.2). By specifying a hue parameter (e.g., Tumor Type), we were able to incorporate a meaningful association using this method. Consequently, we transformed the default marginal plot into a layered KDE plot. This approach tackles the challenge of reconstructing the density function  $f$  using an independent and identically distributed (iid) sample  $x_1, x_2, \dots, x_n$  from the respective probability distribution.

## 2.7 Machine Learning

To decrease overfitting and convergence issue of counterfactuals, especially for EP, we took less patients to implement the task: 25 patients from MB, PA and BG and 11 patients from EP. For testing, to ensure the reliability of our ML models, particularly with a small dataset, we conducted five runs using stratified random sampling based on tumor type with 55% train and 45% test patients.

Using nine ML models, including support vector machine (SVM), adaboost (ADA), logistic regression (LR), random forest classifier (RF), decision tree classifier (DT), gradient boosting classifier (GB), catboost classifier (CB), extreme gradient boosting classifier (XGB) and voting classifier (VOTING), we evaluated the models on the raw data with the outcomes prior to our counterfactual interpretations. CB and XGB were obtained from CatBoost version 1.1.1 and XGBoost version 1.5.1 libraries, respectively, while the other models were obtained from the Scikit-Learn library.

We assessed the performance of the models using precision, recall, and F1 score, which were calculated based on the counts of true positives (TP), true negatives (TN), false positives (FP), and false negatives (FN). In order to ensure an accurate interpretation of the ML results, we opted not to balance the labels. Instead, we employed macro precision, macro recall, and macro F1 score metrics, which take into account the contributions of all labels equally. This approach enabled us to observe the genuine impact of the varying label frequencies, EP in this case.

The validation metrics used in ML are as follows:

$$\text{Macro Precision} = \frac{1}{n} \sum_{i=1}^n \frac{\text{TP}_i}{\text{TP}_i + \text{FP}_i} \quad (3)$$

$$\text{Macro Recall} = \frac{1}{n} \sum_{i=1}^n \frac{\text{TP}_i}{\text{TP}_i + \text{FN}_i} \quad (4)$$

$$\text{Macro F1 Score} = \frac{1}{n} \sum_{i=1}^n \frac{2 \times \text{TP}_i}{2 \times \text{TP}_i + \text{FP}_i + \text{FN}_i} \quad (5)$$

where  $n$  represents the total number of classes or categories.

## 3 Counterfactual Explanations

Given the challenges associated with local approximations, it is worthwhile to explore prior research in the "explanation sciences" to identify potential alternative strategies for generating reliable and practical post-hoc interpretations that benefit the stakeholders affected by algorithmic decisions [1, 41]. To create explanations that are understandable and useful for both experts and non-experts, it is logical to investigate theoretical and empirical studies that shed light on how humans provide and receive explanations [42]. Over the past few decades, the fields of philosophy of science and

epistemology have shown increasing interest in theories related to counterfactual causality and contrastive explanations [41, 43–46].

In philosophy, counterfactuals serve not only to assess the relationship between a mental state and reality, but also to determine whether a mental state can be considered as knowledge. The problem of identifying knowledge with justified true belief is complicated by various counterexamples, such as Gettier cases (1963) [47]. However, some scholars proposed additional conditions to address these counterexamples. This literature highlighted two significant counterfactual conditions:

**Sensitivity:** If  $\rho$  were false,  $\mathcal{S}$  would not believe that  $\rho$ .

**Safety:** If  $\mathcal{S}$  were to believe that  $\rho$ ,  $\rho$  would not be false.

\*Both of these conditions express the notion that  $\mathcal{S}$ 's beliefs must be formed in a manner that is sensitive to the truthfulness of  $\rho$ . The counterfactual semantics has influenced from this idea in various ways, including the establishment of their non-equivalence, clarification, and resolution of potential counterexamples.

This concept has sparked a fresh wave of counterfactual analyses that employ new methodologies. Hitchcock [48, 49] and Woodward [50], for instance, constructed counterfactual analyses of causation using Bayesian networks (also known as "causal models") and structural equations. The basic idea of the analysis can be summarized as follows: " $\mathcal{X}$  can be considered a cause of  $\mathcal{Y}$  only if there exists a path from  $\mathcal{X}$  to  $\mathcal{Y}$ , and changing the value of  $\mathcal{X}$  alone results in a change in the value of  $\mathcal{Y}$ ".

Ginsberg (1986) [51] initiated his discussion by outlining the potential significance of counterfactuals in artificial intelligence and summarizing the philosophical insights that have been drawn regarding them. Following this, Ginsberg provided a structured explanation of counterfactual implication and analyzed the challenges involved in executing it. Over time, numerous developments in the fields of artificial intelligence and cognitive science, including the Bayesian epistemology approach, have gone beyond what was previously envisioned by Ginsberg regarding the potential application of artificial intelligence and counterfactuals [7, 42, 52–55]. Furthermore, Verma et al. [56] conducted a comprehensive review of the counterfactual literature, analyzing its utilization in over 350 research papers.

In recent times, there has been a growing interest in the concept of counterfactual explanations, which aim to provide alternative perturbations capable of changing the predictions made by a model. In simple terms, when given an input feature  $x$  and the corresponding output produced by an ML model  $f$ , a counterfactual explanation involves modifying the input to generate a different output  $y$  using the same algorithm. To further explain this concept, Wachter et al. [7] introduce the following formulation in their proposal:

$$c = \arg \min_c \ell(f(c), y) + |x - c| \quad (6)$$

The initial component  $\ell$  of the formulation encourages the counterfactual  $c$  to deviate from the original prediction, aiming for a different outcome. Meanwhile, the second component ensures that the counterfactual remains in proximity to the original instance, thereby emphasizing the importance of maintaining similarity between the two.

### 3.1 Generating Counterfactual Explanations

The argument of causality in counterfactuals applies to various situations that involve making decisions about an individual's future, like determining admission to a university [57], distributing government aid [58, 59], evaluating job applicants [60], and identifying those at risk of future illnesses [61]. In similar events to these, if the received response is *negative*, it is not sufficient to only learn that the response is *negative*; it is quite important to understand how the results can be improved or modified in the future without making significant and unrealistic changes to the data.

Furthermore, we propose that counterfactual explanations can effectively utilize factual knowledge obtained from MRI features. These features serve as differentiators for distinct tumors, enabling the differentiation between two tumors with minimal adjustments. In essence, this approach aims to identify the most distinguishing characteristics when comparing tumors. This methodology becomes especially valuable when conventional diagnostic methods struggle to differentiate between tumor types. By integrating interpretations and explanations into ML models, we have the potential to identify key features that contribute to accurate tumor classification and, ultimately, improve patient outcomes.

The concept of *data manifold* proximity, as depicted in Fig. 1, is an important constraint that needs to be carefully addressed. It is important to have confidence in the credibility of a counterfactual explanation, which entails generating a set of features that bear resemblance to prior observations encountered by the classifier. If a counterfactual produces unrealistic features that diverge from the training data or disrupt the observed associations between features, it would be considered impractical and outside the norm established by the training data points [62]. Hence, it is essential to ensure

\*<https://plato.stanford.edu/entries/counterfactuals>

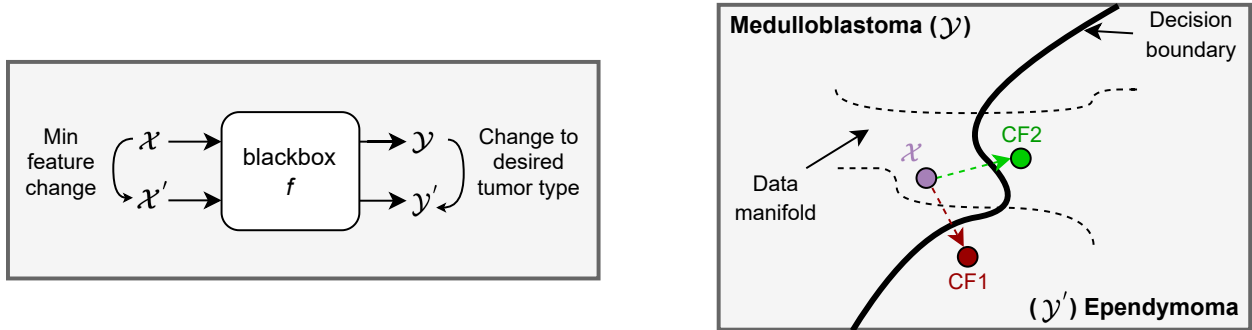


Figure 1: The illustration of generating counterfactual explanations on tumor types. The figure on the left depicts the process of manipulating features and outcomes using a black-box ML model with a counterfactual approach. On the right-hand side, a more detailed depiction of what happens during this process and the concept of "counterfactual explanation" is shown with two example tumor types. The green (CF2) is valid counterfactual, while the red (CF1) is representing fanciful generation.

that generated counterfactuals are realistic, closely aligning with the training data and preserving the observed feature associations. To address this issue, several methods, including constraint-based approaches, have been consciously integrated into algorithms. For instance, changing the "age" and "gender" parameters would be highly unreasonable; therefore, we specify this in the model and prevent counterfactual from deviating from reality. In this research, we impose restrictions on parenchyma features, which serve as a reference point for tissue characteristics. We integrated parenchyma features during the training phase, but they were constrained from being modified during the counterfactual generation process.

Diverse Counterfactual Explanations (DiCE<sup>†</sup>) [63] library provides us with easy-to-use and modifiable code to accomplish this task. DiCE utilizes cutting-edge research to generate counterfactual explanations for any ML model. The main concept is to frame the process of finding these explanations as an optimization problem, similar to how adversarial examples are found (e.g., DeepFool [64]). However, the crucial distinction is that for explanations, we require perturbations that not only alter the output of the ML model but are also varied and realistic to implement.

The counterfactual generation engine of DiCE incorporates diversity and feasibility constraints, which involve several factors: diversity through determinantal point processes, proximity, sparsity, and user constraints. Subsequently, an optimization formula was proposed as follows:

$$C(x) = \arg \min_{c_1, \dots, c_k} \frac{1}{k} \sum_{i=1}^k \ell(f(c_i), y) + \frac{\lambda_1}{k} \sum_{i=1}^k \text{dist}(c_i, x) - \lambda_2 \text{dpp\_diversity}(c_1, \dots, c_k), \quad (7)$$

where the function  $\ell$  was chosen as hinge loss,

$$\ell = \max(0, 1 - z * \text{logit}(f(c))), \quad (8)$$

where  $z$  is assigned a value of -1 when  $y$  equals 0, and a value of 1 when  $y$  equals 1. The term  $\text{logit}(f(c))$  refers to the unscaled output generated by the ML model. For instance, it represents the final logits that are input into a softmax layer to facilitate predictions within a neural network.

dpp\_diversity represented as,

$$\text{dpp\_diversity} = \det(K), \quad (9)$$

where  $K_{i,j} = \frac{1}{1 + \text{dist}(c_i, c_j)}$  and  $\text{dist}(c_i, c_j)$  indicates a measurement of distance between the two counterfactual examples. Further details of the formula and evaluation can be found at [63].

## 4 Results

### 4.1 What if the counterfactual explanations graciously provide us with additional insights into classification?

DiCE provides multi-class training capability, allowing us to develop a framework that facilitates joint training and response acquisition for all four tumor types. Fig. 1 illustrates the visualization of idea for binary classification. This

<sup>†</sup><https://github.com/interpretml/DiCE>

framework aims to leverage counterfactual explanations, acting as a classifier, to determine the tumor type that best aligns with the numerical MRI data of a newly arrived patient. Furthermore, it strives to uncover the factors and distinctive characteristics that differentiate this tumor type from others, even when only numeric MRI data is available for the patient.

By utilizing all four tumor types, we essentially construct a decision space of reality with our existing patients. As the new patient is guided through this space, attempting to transform into each disease sequentially, the degree of self-modification required for each specific tumor condition will vary. As the required changes decrease, it can be inferred that the patient is closer to that particular tumor type since they necessitate fewer modifications. Similarly, understanding the level of dissimilarity and the contributing features to this dissimilarity has been explored as a critical approach in determining the tumor type.

Our approach for using counterfactual explanations as classifiers avoids the need to separate different test sets. As a result, performance of ML models significantly surpasses the baseline scores, with only a few patients excluded from the decision space to simulate the scenario of newly arriving patients. In this case, all train samples become test patients, as we explore the decision space. To achieve this, DiCE provides valuable information regarding misclassified samples, enabling us to exclude the associated counterfactuals from the statistical analysis through post-processing.

The LR model outperformed other models in overall performance. Furthermore, when we experimented with alternative models for generating counterfactuals, we observed that a larger number of patients failed to converge to the target disease compared to LR. This situation made it challenging to write an automated code for entire patients using DiCE when analyzing counterfactuals. LR resolved this issue since it was able to converge for the transformation of all the provided patients. Therefore, we decided to continue using LR for generating counterfactuals.

Figure 2 and Table 1 illustrate the concept of using counterfactuals as a classifier. This approach can be explained as follows: We have a newly arrived patient who has undergone only an MRI scan, and it is not possible to determine the type of tumor based solely on the MRI images. Our approach aims to generate alternative realities or what-if? scenarios (e.g., "what if we had MB? how much would it change?" or "what if we had EP?") for patient  $x$  by utilizing the factual MRI data we possess and leveraging information from the previously obtained decision space. By applying a what-if scenario to each tumor, we can clearly identify which tumor type the available data is closer to or which MRI features need to be adjusted to achieve closer proximity. The overall feature distance, suitably scaled, provides an indication of how different the tumor type of the new patient could be compared to others.

Table 1 provides detailed information about an unknown patient whose ground-truth classification is EP. In case of the MB counterfactual sample, changes are observed in FLAIR\_Tumor and T1CE\_Tumor features, resulting in distances of -663 and 417.5, respectively. As for the EP group, the only noticeable change is observed in the T2\_Tumor feature, with a distance of 137.2. On the other hand, significant changes can be observed for the PA group in the T2\_Tumor (1286 to 2290.2), ADC\_Tumor (1.009 to 2), and T1CE\_Tumor (892 to 1492.5) features. Similarly, for the BG group, differences can be observed in DWI\_Tumor (1175 to 544.23), ADC\_Tumor (1.009 to 2), and T1CE\_Ratio (1.595 to 0.781). Based on these findings, it can be inferred that fewer changes are required in our factual data to align with the characteristics of EP. Consequently, we can conclude the presence of EP patients and further investigate the discrepancies in features among other tumor types. Furthermore, Table 2 is included to present additional potential clinical cases. The last patients belonging to each tumor type were chosen and removed from the decision space to assume their current status as unknown cases.

The MB counterfactual sample exhibits differences only in the FLAIR\_Ratio feature, with a change from 1.141 to 0.742. In the case of EP, increases are observed in the FLAIR\_Tumor feature (from 1107 to 2493) and the ADC\_Ratio feature (from 0.87 to 2.316). Similarly, for PA, changes are observed in the T2\_Ratio feature (from 1.638 to 2.61) and the ADC\_Ratio feature (from 0.87 to 2.892). The algorithm selects changes in the ADC\_Tumor feature (from 0.54 to 2.05) and ADC\_Ratio (from 0.87 to 2.917) for the BG group.

In the case of PA, the factual data reveals differences in the T2\_Ratio, FLAIR\_Ratio, ADC\_Tumor, and T1\_Ratio features. Specifically, the changes in the MB counterfactual sample are from 2.297 to 0.97, 1.143 to 0.608, 1.879 to 0.4, and 0.57 to 0.535, respectively. For EP, decreases are observed in the T2\_Tumor (1778 to 913.6), T2\_Ratio (2.297 to 0.968), DWI\_Tumor (809 to 402.32), DWI\_Ratio (0.805 to 0.476), and ADC\_Tumor (1.879 to 0.4) features. Conversely, for PA, no significant changes are observed except for the DWI\_Ratio feature, which changes from 0.805 to 1.025. Regarding the BG group, changes occur in the T2\_Ratio feature (from 2.297 to 1.072) and the T1CE\_Ratio feature (from 1.125 to 0.768).

In the case of the last instance, BG, significant changes are required in almost all features to transform it into an MB patient compared to its factual data. For EP, changes are observed in the T2\_Tumor feature (from 1709 to 860.3), T2\_Ratio feature (from 1.724 to 0.908), FLAIR\_Tumor feature (from 1150 to 2019), and ADC\_Tumor feature (from 1.59 to 0.34). In case of PA, changes occur in the ADC\_Tumor feature (from 1.59 to 1.56) and T1CE\_Tumor feature

1. Using the MRI features of a newly arrived (undiagnosed) patient, finding the closest convenient points to this individual in the decision space to generate alternative realities.

2. Consolidating the individually created explanations for corresponding tumor types to compare them with factual (original data).

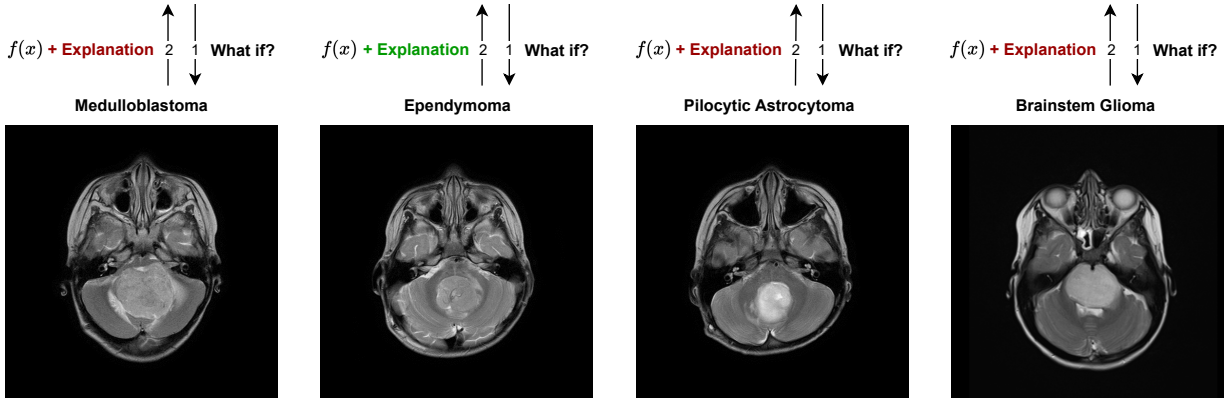


Figure 2: The figure illustrates a clinical scenario demonstrating the practical application of counterfactuals and how they can be utilized in practice.

<b>Factual (<math>x</math>)</b>												
Tumor Type	T2_T	T2_R	FLAIR_T	FLAIR_R	DWI_T	DWI_R	ADC_T	ADC_R	T1_T	T1_R	T1CE_T	T1CE_R
unknown (EP)	1286	1.529	1311	1.341	1175	1.088	1.009	1.771	473	0.84	892	1.595
<b>Counterfactual (<math>x_{cf}</math>)</b>												
Tumor Type	T2_T	T2_R	FLAIR_T	FLAIR_R	DWI_T	DWI_R	ADC_T	ADC_R	T1_T	T1_R	T1CE_T	T1CE_R
MB	-	-	648	-	-	-	-	-	-	-	1309.5	-
EP	1423.2	-	-	-	-	-	-	-	-	-	-	-
PA	2290.2	-	-	-	-	-	2	-	-	-	1492.5	-
BG	-	-	-	-	544.23	-	2	-	-	-	-	0.781

Table 1: This table presents the results of our proposed method utilizing counterfactuals (Fig. 2).

(from 326 to 1234). Conversely, in the BG counterfactual, minimal changes are observed in the features, with only the FLAIR\_Ratio feature undergoing a change from 1.189 to 0.752.

In Tables 1, 2 and 3, T represents Tumor, and R represents Ratio (Tumor/Parenchyma). The variable  $x$  denotes the actual MRI feature values of a new unknown labeled patient. Although we have access to the ground-truth in this testing, we assume that we do not. The variable  $x_{cf}$  represents a hypothetical scenario in which we transform the patient into all possible tumor types to obtain counterfactual outputs. These outputs help us identify which features are similar and need to be altered to correspond to each tumor type. The symbol (-) indicates no modification in the feature. For example, in Table 1, the patient is identified as an EP patient based on having the lowest feature distance overall to the EP type. Thus, we predict that this new patient most likely has EP.

In Table 3, we present the same samples as depicted in Tables 1 and 2, but with standardized features to enable meaningful distance measurements. This explicit representation of tumor classification allows for better comparison. For an actual patient diagnosed as MB, the distance from the counterfactual explanation generated using the MBs is 2.5, and it is close to an EP counterfactual explanation. In the case of a new patient diagnosed as EP, it is 2.985 units away from one of the closest MB counterfactual explanations and 0.35 units away from the generated EP counterfactual. If the patient is diagnosed as PA, it is 3.157 units away from the second closest BG counterfactual explanation and 1.252 units away from the PA counterfactual explanation. Lastly, for a patient diagnosed as BG, the distance from the generated BG counterfactual is 1.853 units, and is 2.574 units away from one of the closest PA counterfactual explanations. The data represented by (-) actually have the same values as the original data and are included for simplification and clearer representation. The distance metric used is generally independent of the results and only alters the magnitude of distances between them.

	Tumor Type	T2_T	T2_R	FLAIR_T	FLAIR_R	DWI_T	DWI_R	ADC_T	ADC_R	T1_T	T1_R	T1CE_T	T1CE_R
<i>Factual (x)</i>	<i>unknown (MB)</i>	1534	1.638	1107	1.141	1883	1.614	0.54	0.87	513	0.842	818	1.327
Counterfactual ( $x_{cf}$ )	MB	-	-	-	0.742	-	-	-	-	-	-	-	-
Counterfactual ( $x_{cf}$ )	EP	-	-	2493	-	-	-	-	2.316	-	-	-	-
Counterfactual ( $x_{cf}$ )	PA	-	2.61	-	-	-	-	-	2.892	-	-	-	-
Counterfactual ( $x_{cf}$ )	BG	-	-	-	-	-	-	2.05	2.917	-	-	-	-
<i>Factual (x)</i>	<i>unknown (PA)</i>	1778	2.297	1085	1.143	809	0.805	1.879	2.685	439	0.57	747	1.125
Counterfactual ( $x_{cf}$ )	MB	-	0.967	-	0.608	-	-	0.4	-	-	0.535	-	-
Counterfactual ( $x_{cf}$ )	EP	913.6	0.968	-	-	402.32	0.476	0.4	-	-	-	-	-
Counterfactual ( $x_{cf}$ )	PA	-	-	-	-	-	1.025	-	-	-	-	-	-
Counterfactual ( $x_{cf}$ )	BG	-	1.072	-	-	-	-	-	-	-	-	-	0.768
<i>Factual (x)</i>	<i>unknown (BG)</i>	1709	1.724	1150	1.189	1112	0.674	1.59	2.148	373	0.643	326	0.652
Counterfactual ( $x_{cf}$ )	MB	1000.9	-	974	0.669	-	-	0.5	0.677	1424	0.573	479.9	0.76
Counterfactual ( $x_{cf}$ )	EP	860.3	0.908	2019	-	-	-	0.34	-	-	-	-	-
Counterfactual ( $x_{cf}$ )	PA	-	-	-	-	-	-	1.56	-	-	-	1234	-
Counterfactual ( $x_{cf}$ )	BG	-	-	-	0.752	-	-	-	-	-	-	-	-

Table 2: The table presents additional counterfactual cases generated for different newly arriving patients. The Tumor and Ratio features are not on the same scale for direct comparison due to their mathematical dependency.

	Tumor Type	T2_T	T2_R	FLAIR_T	FLAIR_R	DWI_T	DWI_R	ADC_T	ADC_R	T1_T	T1_R	T1CE_T	T1CE_R	Distance
<i>Factual (x)</i>	<i>unknown (MB)</i>	0	-0.5	-0.5	0.5	0	0	-0.5	-1.191	0	0	0	0	-
Counterfactual ( $x_{cf}$ )	MB	-	-	-	-2	-	-	-	-	-	-	-	-	<b>2.5</b>
Counterfactual ( $x_{cf}$ )	EP	-	-	2	-	-	-	-	0.370	-	-	-	-	2.948
Counterfactual ( $x_{cf}$ )	PA	-	2	-	-	-	-	-	0.993	-	-	-	-	3.319
Counterfactual ( $x_{cf}$ )	BG	-	-	-	-	-	-	2	1.020	-	-	-	-	3.337
<i>Factual (x)</i>	<i>unknown (EP)</i>	-0.583	0	0.5	0	0.5	0	-0.816	0	0	0	-0.795	0.5	-
Counterfactual ( $x_{cf}$ )	MB	-	-	-2	-	-	-	-	-	-	-	0.836	-	2.985
Counterfactual ( $x_{cf}$ )	EP	-0.233	-	-	-	-	-	-	-	-	-	-	-	<b>0.350</b>
Counterfactual ( $x_{cf}$ )	PA	1.982	-	-	-	-	-	1.225	-	-	-	1.550	-	4.031
Counterfactual ( $x_{cf}$ )	BG	-	-	-	-	-2	-	1.225	-	-	-	-	-2	4.082
<i>Factual (x)</i>	<i>unknown (PA)</i>	0.5	1.223	0	0.5	0.5	0.124	0.816	0	0	0.5	0	0.5	-
Counterfactual ( $x_{cf}$ )	MB	-	-0.871	-	-2	-	-	-1.225	-	-	-2	-	-	4.588
Counterfactual ( $x_{cf}$ )	EP	-2	-0.869	-	-	-2	-1.749	-1.225	-	-	-	-	-	4.955
Counterfactual ( $x_{cf}$ )	PA	-	-	-	-	-	1.377	-	-	-	-	-	-	<b>1.252</b>
Counterfactual ( $x_{cf}$ )	BG	-	-0.705	-	-	-	-	-	-	-	-	-	-2	3.157
<i>Factual (x)</i>	<i>unknown (BG)</i>	0.811	0.5	-0.373	0.811	0	0	0.831	0.5	-0.5	0.5	-0.602	-0.5	-
Counterfactual ( $x_{cf}$ )	MB	-1.033	-	-0.847	-1.393	-	-	-1.079	-2	2	-2	-0.166	2	6.109
Counterfactual ( $x_{cf}$ )	EP	-1.400	-2	1.966	-	-	-	-1.360	-	-	-	-	-	4.627
Counterfactual ( $x_{cf}$ )	PA	-	-	-	-	-	-	0.778	-	-	-	1.971	-	2.574
Counterfactual ( $x_{cf}$ )	BG	-	-	-	-1.041	-	-	-	-	-	-	-	-	<b>1.853</b>

Table 3: Distance results for counterfactuals generated on feature-wise scaled data for four distinct newly arriving patients with varying tumor types.

## 4.2 Revealing Key MRI Features through Counterfactual Explanations

As discussed in Section 3.1, counterfactual explanations can provide insights into feature importance. These explanations allow us to understand the reasoning behind ML model decisions and offer valuable options for restriction. In clinical settings, visible changes in features through counterfactual explanations can be more relevant and meaningful for real-world evaluations and applications.

Considering that we generated five counterfactuals for each patient, we obtained 125 explanations for MB, PA, and BG, and 55 explanations for EP. Table 4 illustrates our reporting method for counterfactual analysis results for a case scenario (MB to EP). The patient count, the total number of generated counterfactual explanations for them, and the statistical information regarding the frequency of changes observed on which features in these counterfactuals to identify the top 3 influential features are shown. For instance, "FLAIR\_Tumor 71 changes" signifies that out of 125 counterfactuals, 71 of them involved a modification from MB to EP. Therefore, FLAIR\_Tumor creates such a distinction between these two tumors that the model considers altering this feature significantly influential in shifting the decision from one side to the other in the decision space. The greater the repetition of this occurrence, indicated by the magnitude of "changes," the more pronounced the outcome suggesting that even in random selections, optimization is achieved for that particular feature, significantly impacting the decision.

Table 5 presents the findings from each tumor pair to identify feature differences between different tumor types. The observed changes in features align with expected outcomes from clinical studies. MB and EP tumors are distinguished

Number of patients: 25

Number of generated counterfactuals: 125

FLAIR_Tumor	71 changes	T1_Ratio	6 changes
ADC_Tumor	33 changes	T1CE_Tumor	6 changes
ADC_Ratio	29 changes	T2_Tumor	3 changes
DWI_Ratio	18 changes	T2_Parenchyma	0 changes
FLAIR_Ratio	17 changes	FLAIR_Parenchyma	0 changes
DWI_Tumor	12 changes	DWI_Parenchyma	0 changes
T1_Tumor	10 changes	ADC_Parenchyma	0 changes
T1CE_Ratio	7 changes	T1_Parenchyma	0 changes
T2_Ratio	6 changes	T1CE_Parenchyma	0 changes

Table 4: This example analysis presents the variations in characteristics observed during the generation of counterfactual instances for the transition from MB to EP.

by FLAIR and ADC features. MB and PA typically exhibit differences in T2 and ADC. MB and BG, on the other hand, show variations primarily in ADC, T2, and T1CE. In the case of EP and PA, T2 exhibits the most significant changes, while variations in ADC and T1CE are also observed. The most distinguishing features between EP and BG are T1CE\_Ratio and ADC\_Tumor. As for PA and BG, the T2\_Ratio feature has been identified as a crucial factor in creating differentiation. Additionally, significant variations in T1CE features are frequently observed, further contributing to the dissimilarity between these tumor types.

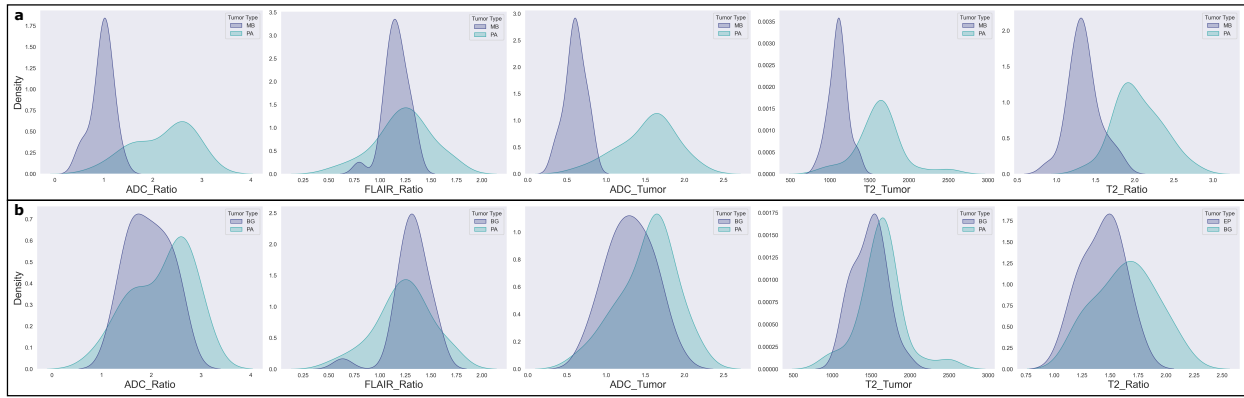


Figure 3: Original data distributions for MB - PA and BG - PA, focusing on specific features.

The results presented in Table 5, along with the visualization in Fig. 3, provide insights into the PA example as follows: When considering the scenarios of MB to PA or PA to MB, it is generally observed that similar distributions dominate. The distinctiveness of the distributions between MB and PA becomes evident when examining the top 5 features that exhibit the most variation, as shown in Fig. 3 and discussed in our previous study [65]. Furthermore, when examining nearly identical distributions between BG and PA, a lack of discernibility is found. This is further supported by the absence of these features among the important features for BG to PA or PA to BG, as demonstrated in Table 5. These findings indicate that the algorithm effectively operates in accordance with our expectation during counterfactual generation, which involves altering the most distinct features to achieve maximum impact with minimal modification. Notably, T1CE features and T2\_Ratio are identified as the most distinctive features between BG and PA, as shown in Fig. 5 of [65].

This understanding supports the notion that the top 3 features with the most distinct distributions in KDE plots are indeed the most discriminative features. It also corroborates our previous study [65], which employed a different explanatory approach. Additionally, this concept provides numerous additional findings that can be interpreted in conjunction with our prior work. Furthermore, in addition to our previous proposition, the nature of the variation in counterfactual explanations inherently identifies the features that will have the greatest impact. This reveals that the most changing features in generating different counterfactual explanations for patients actually correspond to the features that contribute the most to the dissimilarity between the two tumor types.

MB to EP		MB to PA		MB to BG		EP to MB		EP to PA		EP to BG	
Feature	Change	Feature	Change	Feature	Change	Feature	Change	Feature	Change	Feature	Change
FLAIR_Tumor	71	T2_Ratio	87	T2_Tumor	64	T1CE_Tumor	18	T2_Tumor	34	ADC_Tumor	22
ADC_Tumor	33	T2_Tumor	55	ADC_Tumor	52	FLAIR_Ratio	16	T2_Ratio	26	DWI_Ratio	16
ADC_Ratio	29	ADC_Tumor	43	T1CE_Ratio	43	FLAIR_Tumor	13	ADC_Tumor	19	T1CE_Ratio	15

PA to MB		PA to EP		PA to BG		BG to MB		BG to EP		BG to PA	
Feature	Change	Feature	Change	Feature	Change	Feature	Change	Feature	Change	Feature	Change
ADC_Ratio	91	T2_Ratio	95	T2_Ratio	95	FLAIR_Ratio	85	T1CE_Ratio	90	T1CE_Ratio	53
FLAIR_Ratio	88	T2_Tumor	81	T1CE_Tumor	66	ADC_Tumor	71	T1_Tumor	50	T1CE_Tumor	48
ADC_Tumor	76	T1CE_Tumor	45	T1CE_Ratio	54	ADC_Ratio	71	DWI_Ratio	48	T2_Ratio	32

Table 5: The three most important features for each changing reality case.

### 4.3 Statistical Analysis of Generated Counterfactuals

During the construction of the counterfactual tumor  $y$  from the original tumor  $x$ , we conducted a dependent test to assess the statistical difference between  $x$  and  $y$ , as explained in Section 2.5. Apart from the PA to MB transition (e.g.,  $p=0.04763$ ,  $p=0.0307$ ), no significant differences were observed in other tumor transitions. This result can be attributed to both the fundamental optimization principle of minimizing changes during counterfactual generation and the distribution distances shown in Fig. 3. Specifically, Fig. 3a demonstrates a distinct separation in the distributions during the PA to MB transition, requiring a significantly larger change for transformation.

Table 6 presents the statistical similarity obtained when each tumor is transformed to represent the "what if?" scenario of other tumors. In other words, when we transform tumor  $x$  to tumor  $x'=y$ , we know that  $x'$  is still dependent on  $x$ .

MRI Feature	Original	Generated	T-Statistic	P-Value	MRI Feature	Original	Generated	T-Statistic	P-Value
DWI_Tumor	MB	MB to MB	-0.0605	0.9521	FLAIR_Tumor	EP	MB to EP	-3.2397	0.0061
T1CE_Ratio	MB	MB to MB	-0.3643	0.7177	ADC_Tumor	EP	MB to EP	-2.0273	0.0495
T1_Ratio	MB	MB to MB	-0.0282	0.9776	ADC_Ratio	EP	MB to EP	-0.6434	0.5266
T1CE_Tumor	MB	EP to MB	-2.4975	0.0156	FLAIR_Tumor	EP	EP to EP	-1.0603	0.3018
FLAIR_Ratio	MB	EP to MB	0.4532	0.6524	ADC_Tumor	EP	EP to EP	-1.4653	0.1519
FLAIR_Tumor	MB	EP to MB	0.7917	0.4331	DWI_Ratio	EP	EP to EP	-0.4937	0.6278
ADC_Ratio	MB	PA to MB	-0.4017	0.6887	T2_Ratio	EP	PA to EP	2.956	0.007
FLAIR_Ratio	MB	PA to MB	11.5615	<0.0001	T2_Tumor	EP	PA to EP	0.3621	0.72
ADC_Tumor	MB	PA to MB	-4.3706	<0.0001	T1CE_Tumor	EP	PA to EP	-1.1672	0.262
FLAIR_Ratio	MB	BG to MB	6.7026	<0.0001	T1CE_Ratio	EP	BG to EP	-2.1967	0.0428
ADC_Tumor	MB	BG to MB	-5.2062	<0.0001	T1_Tumor	EP	BG to EP	-5.9549	<0.0001
ADC_Ratio	MB	BG to MB	-2.7487	0.0071	DWI_Ratio	EP	BG to EP	0.0059	0.9954

(a) Difference between original MB and generated MBs.

(b) Difference between original EP and generated EPs.

MRI Feature	Original	Generated	T-Statistic	P-Value	MRI Feature	Original	Generated	T-Statistic	P-Value
T2_Ratio	PA	MB to PA	-2.0667	0.0430	T2_Tumor	BG	MB to BG	-2.4723	0.0149
T2_Tumor	PA	MB to PA	-0.1256	0.9004	ADC_Tumor	BG	MB to BG	5.6539	<0.0001
ADC_Tumor	PA	MB to PA	4.4019	<0.0001	T1CE_Ratio	BG	MB to BG	-6.6115	<0.0001
T2_Tumor	PA	EP to PA	-1.3925	0.1694	ADC_Tumor	BG	EP to BG	2.8215	0.0066
T2_Ratio	PA	EP to PA	1.6279	0.1091	DWI_Ratio	BG	EP to BG	0.806	0.4236
ADC_Tumor	PA	EP to PA	3.6692	0.0005	T1CE_Ratio	BG	EP to BG	-4.4199	<0.0001
ADC_Tumor	PA	PA to PA	0.2781	0.7822	T2_Ratio	BG	PA to BG	6.78	<0.0001
T1_Ratio	PA	PA to PA	-0.8599	0.3948	T1CE_Tumor	BG	PA to BG	-5.3162	<0.0001
FLAIR_Tumor	PA	PA to PA	-1.2497	0.2176	T1CE_Ratio	BG	PA to BG	-6.9185	<0.0001
T1CE_Ratio	PA	BG to PA	1.711	0.0944	ADC_Tumor	BG	BG to BG	-0.3252	0.7467
T1CE_Tumor	PA	BG to PA	1.7524	0.0862	DWI_Tumor	BG	BG to BG	-0.8181	0.4176
T2_Ratio	PA	BG to PA	2.2029	0.0326	DWI_Ratio	BG	BG to BG	-0.7461	0.4599

(c) Difference between original PA and generated PAs.

(d) Difference between original BG and generated BGs.

Table 6: The results of hypothesis tests comparing the original data with the generated data.

Therefore, we measure how similar  $x'$  is to the original distribution of  $y$  on the feature where  $x$  undergoes the most significant change. A high  $p$ -value indicates that we do not reject the difference, implying that the counterfactual explanations we generate sufficiently resemble the original distribution for that particular feature.

As expected, when attempting self-transformation on each tumor type, the obtained  $p$ -values were notably high. Evaluating at a significance level of 0.05, several features closely aligned with the actual feature distribution of the patients, making them indistinguishable from the ground truth. The following features exhibited this characteristic: FLAIR\_Ratio and FLAIR\_Tumor in the case of transforming EP to MB, ADC\_Ratio when transforming PA to MB, ADC\_Ratio during the transformation from MB to EP, T2\_Tumor and T1CE\_Tumor in the context of PA to EP transformation, DWI\_Ratio when transforming BG to EP, T2\_Tumor for MB to PA transformation, T2\_Tumor and T2\_Ratio in the case of EP to PA transformation, T1CE\_Ratio and T1CE\_Tumor during BG to PA transformation, and DWI\_Ratio when transforming EP to BG. Fig. 4 presents some of these cases along with their KDE distributions.

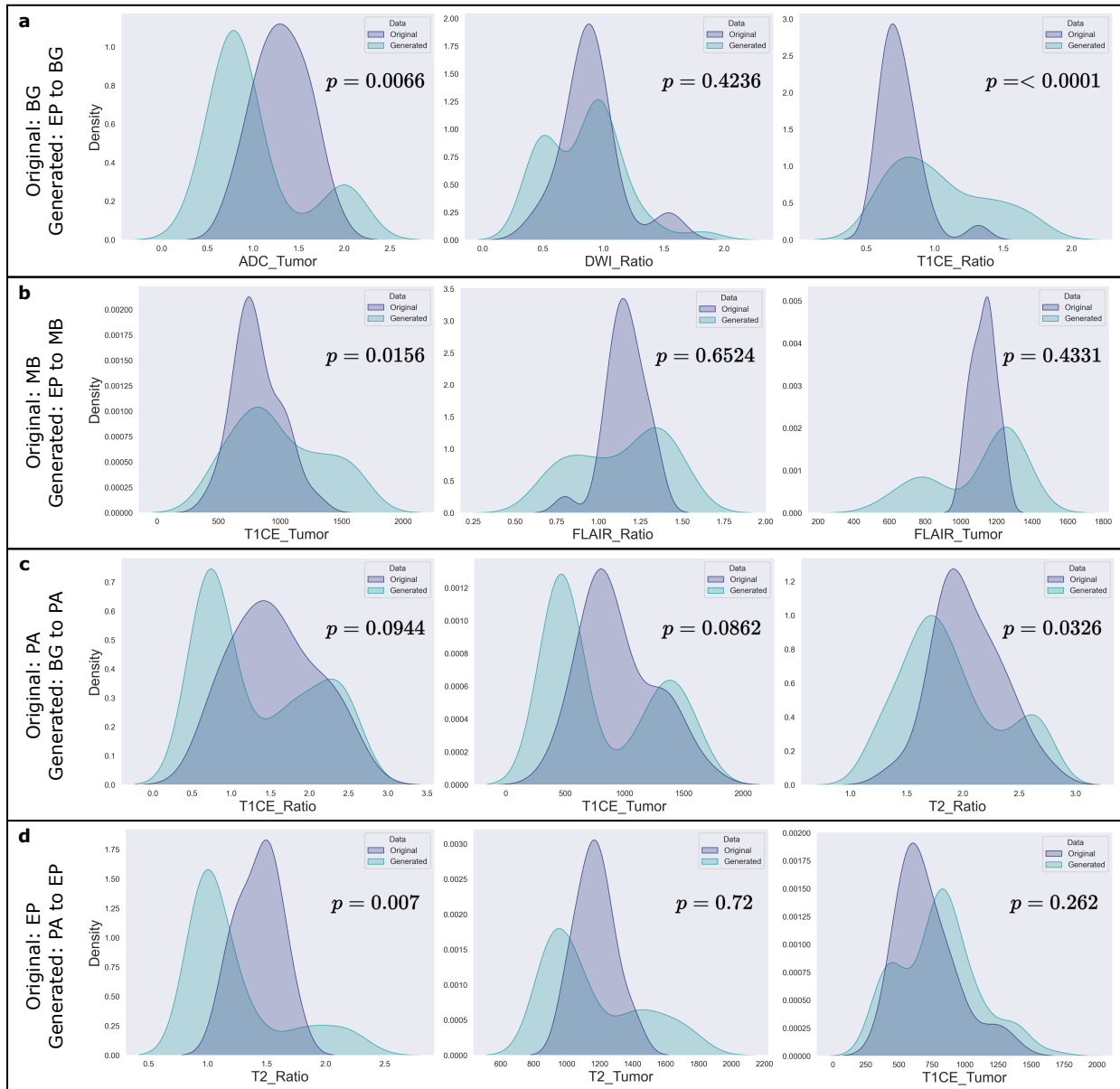


Figure 4: The distributions of the original data and the generated data.

#### 4.4 Pushing the Boundaries of Data Augmentation through Alternative Realities

During the construction of counterfactuals, we employed downsampling for MB and BG to align with the number of PA patients (25) during training, considering it appropriate. EP had a count of 11, and we did not increase it. The baseline results for this scenario can be observed in Table 7. For evaluation, the train-test splitting was conducted with a ratio of 45% for the baseline dataset, 35% for EP augmentation, and 25% for EP-PA-BG augmentation.

	Precision	Recall	F1 Score
Baseline	73.15 $\pm$ 9.48	72.20 $\pm$ 4.78	71.28 $\pm$ 5.62
A	84.83 $\pm$ 4.95	83.75 $\pm$ 3.72	83.34 $\pm$ 3.65
B	86.31 $\pm$ 4.57	84.64 $\pm$ 4.69	84.85 $\pm$ 4.72
C	73.58	72.73	72.04

Table 7: The impact of data augmentation using counterfactuals on classification scores is presented in the table. **(A)** For the first augmentation scenario, only EP counterfactuals are added, resulting in a dataset with 25 samples each for MB, EP, PA, and BG. **(B)** In the second augmentation scenario, counterfactuals for EP, PA, and BG are added to balance the number of samples with original count of MB. Assuming all counterfactual examples represent real data, this scenario results from a dataset comprising 42 samples each for MB, EP, PA, and BG. **(C)** The third scenario involves moving all real samples to the test set, with 11 patients in each category. Consequently, no factual EP samples are left in the training set, and the model is trained accordingly. In all cases, LR consistently yields the best results, and all the reported results in the table are from the LR classifier.

To address the data imbalance, we examined the inclusion of generated counterfactuals for data augmentation. For example, by equalizing EP with the other tumor types and incorporating 14 different generated counterfactuals alongside the originals, we excluded EP-to-EP instances. Opting for transitions from various tumor types to maximize variance and generalizability, we achieved an improvement of up to 12.06% as shown in Table 7, case A.

To incorporate the previously set aside MB and BG data, we aligned all tumor types, except themselves, with counterfactuals generated from different tumor types. BG, PA, and EP were included with MB, and all were evaluated as a group of 42 patients, which was the maximum patient count for one tumor type. When considering the counterfactuals as actual patients, the outcomes align with the results presented in Table 7, case B.

Furthermore, in the case examined in Table 7, case C, 11 patients were included from each tumor type in the test set, resulting in no actual EP patients in the training set. Consequently, during training, we had 31 real samples for MB, 0 real and 31 counterfactual samples for EP, 14 real and 17 counterfactual samples for PA, and 23 real and 8 counterfactual samples for BG. Notably, when evaluating on real samples, the results were intriguing. Despite the absence of real EP patients in the training data, the model successfully identified 5 out of the 11 patients, leading to an overall baseline score that was, on average, 0.76% higher.

## 5 Discussion

The spatial heterogeneity in tumor characteristics presents a substantial clinical challenge in pediatric brain tumors. Specifically, tumors originating from the posterior fossa often exhibit overlapping imaging features, leading to difficulties in accurate differentiation, even for experienced clinicians. Accurate diagnosis is of paramount importance as each tumor type requires specific treatment strategies, directly impacting patient outcomes and overall quality of life. Despite the promising advancements in AI and medical imaging, the inherent black-box nature of most models and the challenges in convincing clinicians for everyday use often restrict these studies to the realm of research. It is crucial to aspire for these developments to become interactive and trustworthy tools that clinicians can readily utilize in real-life scenarios. Hence, our study introduces a novel approach to the existing literature, offering valuable insights into the underlying patterns and relationships among the features observed in MRI scans. We hypothesize that exploring "what if?" scenarios can significantly enhance our understanding of alternative outcomes and their implications for clinical decision-making. To the best of our knowledge, this research represents a pioneering effort in the investigation of pediatric brain tumors, highlighting its substantial influence on the interpretability and generalizability of ML models in this domain. By exploring alternative scenarios and their impact, we aim to contribute to the advancement of precise diagnostics and improve patient care in this challenging field.

The primary objective of this study was to enhance the interpretability of ML models' outcomes and provide additional insights using a novel approach. Despite being debated in the fields of philosophy and psychology for half a century,

the core idea of counterfactuals has been employed in the field of artificial intelligence under various names, and their complete implementation is relatively recent. In this study, we transformed this idea into the clinical literature to extract valuable information that could be beneficial for clinicians in real-life scenarios. We aim to demonstrate both the alternative possibilities in the decision space and the underlying reasons behind the selected decision by utilizing alternative realities. To achieve this, we perturbed the original data by imposing various constraints during a relatively straightforward mathematical optimization process.

The generated counterfactual explanations provide evidence that there is not always a single definitive choice in life. When considering the diversity in individuals' biological characteristics, it becomes apparent that approaching each case may require a personalized approach. This notion aligns with the concept of personalized healthcare, which has been extensively explored in the health literature [66–69]. In other words, our approach involves producing explanations tailored to each newly arrived patient by drawing insights from previous patients. By leveraging the decision space, we can identify the closest data points in terms of biological characteristics to the newly arrived patient and construct alternative realities specific to that individual. These alternative scenarios allow us to observe the differences in the tumor on the MRI and gain insights into which tumor type it is most closely related to.

As there were no existing counterfactual studies in the literature regarding PF tumors, our study aimed to bridge this gap by subjecting the obtained outputs to various statistical tests. The objective was to provide a comprehensive exploration of the subject matter for enhanced clarity. We specifically investigated two aspects: first, the potential utilization of the generated counterfactuals as a post-classifier, and second, whether they could reveal significant MRI features associated with the corresponding tumor. These investigations were conducted with meticulous attention. Furthermore, we examined the potential impact of reintroducing these diverse counterfactuals into the dataset to address the issue of data imbalance. Statistical tests were also performed to assess the similarity of counterfactuals generated from different spaces to the transformed target space. The results of these tests are presented in Section 4.3.

The LR model exhibited the highest score in our evaluation, and therefore, we utilized it to generate counterfactual explanations. To facilitate the model's learning process and balance the data, we included 11 instances of the EP tumor type while selecting 25 patients from the remaining tumor types, despite there being more instances of certain tumor types.

To automate the generation of counterfactuals for all patients, we developed a framework. However, in cases where an optimal counterfactual explanation cannot be found, the process is halted. Currently, addressing such situations comprehensively is not feasible, and updates are necessary in the DiCE framework. Although we did not encounter this problem with the LR model, as an alternative suggestion, if there is a sufficient number of patients, consider working with a subsample and replace the excluded patients with another patient from the actual population for statistical testing purposes. Instead of employing DiCE, alternative methodologies utilizing various counterfactual algorithmic approaches may be employed, which possess the capability to efficiently address the optimization problem within a more favorable time-interval.

Obtaining specific results for individual patients is not problematic and can be resolved through parameter adjustments or by utilizing different models. However, if the goal is to validate the study and focus on medical research rather than practical outputs, performing a more comprehensive statistical analysis by manually deriving counterfactual explanations for each patient would be less effective and time-consuming. Therefore, as demonstrated in this study, there is a clear need for at least a semi-automated system.

Fig. 2 and Table 1 depict a hypothetical scenario involving a patient with an initially unknown EP tumor. The radiologist examining the MR images was uncertain about whether the tumor was of the MB or EP type. A key challenge in such cases is the lack of additional information, which often necessitates invasive procedures like brain surgery and tissue sampling for histopathological analysis to obtain a definitive diagnosis. To overcome this issue, we generate alternative scenarios based solely on the MRI features. These scenarios provide additional quantitative information to the radiologist, enabling them to assess the response based on the individual's biological characteristics.

Moreover, Table 2 presents examples of other potential tumor cases, while Table 3 demonstrates the efficacy of our approach in identifying patients with diverse tumor types that were previously unidentified and not encompassed within the decision space. While ML models can also accomplish this task, our method offers an additional advantage by preserving information regarding tissue characteristics, which in turn reveal similarities or differences among tumors. Additionally, our approach calculates distances to other tumors by transforming the features into a uniform distribution through standard scaling, providing valuable insights about the proximity. This valuable information aids in our comprehension of the differentiation among tumors in the dataset.

Table 4 presents the total count of modifications made to susceptible features, with the exception of the parenchymas that serves as reference points, when generating samples for different patients. The statistical report enables a human verification of the optimization process, wherein minimal changes are implemented to achieve the desired outcome. It

also confirms that the features exhibiting the highest variations during the generation of alternative realities are those with the most distinct distributions between two tumors. To elucidate the analysis of their distributions, we present Fig. 3 as a visual representation.

Table 5 presents the top three most variable features extracted from the reports obtained for all tumor matches in Table 4. Table 6 exhibits a statistical analysis demonstrating the high degree of similarity between the generated data and reality across different data spaces, specifically focusing on the most frequently selected features. A high  $p$ -value indicates that the generated samples cannot be well distinguished, implying the effectiveness of the independent transformation process, which produces significant alternative realities separate from the original space. Fig. 4 illustrates an example of some transformations from Table 6, displaying their corresponding  $p$ -values, as well as the kernel density estimation of the generated data in comparison to the original data.

Ultimately, we investigated the potential of the generated alternative realities for data augmentation. The reliability of data augmentation methods, such as SMOTE [10], is a subject of controversy in medical research due to their algorithmic dependencies and the often insignificant impact of the generated data on the distribution. These kinds of approaches often prioritize test performance improvement, i.e., the concept of any means to improve test performance is acceptable, without considering alignment with reality. As a result, the generated data mostly lacks interpretability and becomes disconnected from real-world scenarios. However, we believe that accepting this approach as universally valid would be misguided. In situations where both the available data and testing conditions are limited, relying solely on these approaches may not be suitable for ensuring generalizability. It is essential to recognize the limitations and potential drawbacks associated with using generated data for generalization purposes. In medical studies with limited data, we propose that the counterfactuals generated can provide an alternative solution to this problem. Table 7 presents the performance evaluation of the data augmentation methods we assessed.

The results presented in Fig. 7, case C cannot be directly compared with the baseline due to the inclusion of additional test patients during the testing phase. However, it is evident that the inclusion of more real test samples leads to a slight improvement under the given training conditions. It is important to acknowledge that some of the EP patients pose challenges in terms of differentiation, as mentioned in [65]. When these difficult patients are included in the training data, it can lead to a significant elevation in scores or if they end up in the test set, they act as unpredictable outliers, negatively impacting the overall results. Despite these challenges, achieving accurate predictions for half of these patients without utilizing any real EP data in the training set is commendable and warrants attention for future research.

Moreover, the incorporation of counterfactual explanations holds potential in identifying and addressing model bias in medical diagnosis. In certain healthcare data scenarios, the removal of constraints, such as gender or ethnicity, which we previously recommended adding to this approach as restrictions, may facilitate the potential development of fairness, transparency, and accountability in algorithmic decision-making processes. However, further research and implementation efforts are required to explore and validate the applicability of counterfactual explanations in addressing model bias in medical research and practice.

There are several limitations that should be considered in the present study. One limitation pertains to the implementation of the DiCE method, which may pose challenges when applied to diverse datasets. The method sometimes requires extensive optimization time and can encounter difficulties in finding a convergence point, potentially hindering the generation of accurate counterfactual explanations. To address this issue, alternative counterfactual explanation methods (e.g., Dutta et al. [70], Maragno et al. [71]) can be explored in conjunction with our proposed approach. For a more comprehensive collection of counterfactual algorithms, readers can refer to Guidotti’s review paper [72]. Additionally, the dataset utilized in this study has limitations in terms of its scope and size. While it included an adequate number of samples for training ML models, it may not fully capture the range of scenarios encountered in clinical practice, thus potentially limiting the generalizability of the findings to other datasets. Furthermore, the dataset only encompassed four specific types of pediatric PF tumors, which may not represent the entire spectrum of pediatric brain tumors. Future studies should consider expanding the sample size and incorporating additional advanced MRI protocols, such as semiquantitative and quantitative perfusion MRI and MR spectroscopy, to gain deeper insights into the diagnostic and prognostic value of MRI features for pediatric PF tumors.

## 6 Conclusion

In conclusion, this paper introduces a novel perspective on interpretability in medical research, focusing on pediatric PF brain tumors as a case study. Leveraging counterfactual explanations, the study offers personalized and context-specific insights, validating predicted outcomes and shedding light on variations in predictions under different circumstances.

The proposed approach shows great promise in enhancing the interpretability of MRI features for medical research studies. By bridging the gap between ML algorithms and clinical decision-making, it has the potential to facilitate

the adoption of advanced computational techniques in medical practice. Clinicians can benefit from valuable insights gained from the generated counterfactual explanations, leading to improved decision-making processes and ultimately better patient outcomes. Notably, the counterfactual explanations generated in this study maintain statistical and clinical fidelity in many cases, underscoring their significance.

To fully realize the potential of this approach, further research and validation are essential. Integrating counterfactual explanations into existing clinical workflows and evaluating their performance in real-world scenarios will be critical to ensuring the reliability and practicality of this method. The continued development and refinement of utilizing counterfactual explanations in MRI-based diagnoses could revolutionize the medical field, benefiting both patients and healthcare providers. Therefore, future studies with larger datasets within the same domain or for different diseases could yield even more robust alternative realities constructed from MRI features. Overall, this study represents a significant step forward in moving beyond known reality and improving the application of ML in medical research and practice.

## 7 Declaration of competing interest

The authors declare that they have no known competing financial interests or personal relationships that could have appeared to influence the work reported in this paper.

## 8 Funding

This work was supported by The Scientific and Technological Research Council of Türkiye (TUBITAK) [2232-118C221].

## 9 Data & Code Availability

The datasets generated and/or analyzed during the current study are not publicly available due to privacy concerns but are available from the corresponding author upon reasonable request.

The source codes of the presented study can be accessed at: <https://github.com/toygarr/counterfactual-explanations-for-medical-research>

## References

- [1] Brent Mittelstadt, Chris Russell, and Sandra Wachter. Explaining explanations in ai. In *Proceedings of the conference on fairness, accountability, and transparency*, pages 279–288, 2019.
- [2] Alfredo Vellido. The importance of interpretability and visualization in machine learning for applications in medicine and health care. *Neural computing and applications*, 32(24):18069–18083, 2020.
- [3] Michele Avanzo, Lise Wei, Joseph Stancanella, Martin Vallieres, Arvind Rao, Olivier Morin, Sarah A Mattonen, and Issam El Naqa. Machine and deep learning methods for radiomics. *Medical physics*, 47(5):e185–e202, 2020.
- [4] Giovanni Cinà, Tabea Röber, Rob Goedhart, and Ilker Birbil. Why we do need explainable ai for healthcare, 2022.
- [5] Marco Tulio Ribeiro, Sameer Singh, and Carlos Guestrin. " why should i trust you?" explaining the predictions of any classifier. In *Proceedings of the 22nd ACM SIGKDD international conference on knowledge discovery and data mining*, pages 1135–1144, 2016.
- [6] Scott M Lundberg and Su-In Lee. A unified approach to interpreting model predictions. *Advances in neural information processing systems*, 30, 2017.
- [7] Sandra Wachter, Brent Mittelstadt, and Chris Russell. Counterfactual explanations without opening the black box: Automated decisions and the gdpr. *Harv. JL & Tech.*, 31:841, 2017.
- [8] Sebastien C Wong, Adam Gatt, Victor Stamatescu, and Mark D McDonnell. Understanding data augmentation for classification: when to warp? In *2016 international conference on digital image computing: techniques and applications (DICTA)*, pages 1–6. IEEE, 2016.
- [9] Hongyi Zhang, Moustapha Cisse, Yann N Dauphin, and David Lopez-Paz. mixup: Beyond empirical risk minimization. *arXiv preprint arXiv:1710.09412*, 2017.

- [10] Nitesh V Chawla, Kevin W Bowyer, Lawrence O Hall, and W Philip Kegelmeyer. Smote: synthetic minority over-sampling technique. *Journal of artificial intelligence research*, 16:321–357, 2002.
- [11] Steven P Meyers, Susan S Kemp, and Robert W Tarr. Mr imaging features of medulloblastomas. *AJR. American journal of roentgenology*, 158(4):859–865, 1992.
- [12] Kelly K Koeller and Elisabeth J Rushing. From the archives of the afip: medulloblastoma: a comprehensive review with radiologic-pathologic correlation. *Radiographics*, 23(6):1613–1637, 2003.
- [13] Kelly K Koeller and Elisabeth J Rushing. From the archives of the afip: pilocytic astrocytoma: radiologic-pathologic correlation. *Radiographics*, 24(6):1693–1708, 2004.
- [14] Kelly K Koeller and Glenn D Sandberg. From the archives of the afip: cerebral intraventricular neoplasms: radiologic-pathologic correlation. *Radiographics*, 22(6):1473–1505, 2002.
- [15] SP Meyers, ZP Khademian, JA Biegel, SH Chuang, DN Korones, and RA Zimmerman. Primary intracranial atypical teratoid/rhabdoid tumors of infancy and childhood: Mri features and patient outcomes. *American Journal of Neuroradiology*, 27(5):962–971, 2006.
- [16] Kiyokazu Arai, Noriko Sato, Jun Aoki, Akiko Yagi, Ayako Taketomi-Takahashi, Hideo Morita, Yoshinori Koyama, Hiroshi Oba, Shogo Ishiuchi, Nobuhito Saito, et al. Mr signal of the solid portion of pilocytic astrocytoma on t2-weighted images: is it useful for differentiation from medulloblastoma? *Neuroradiology*, 48:233–237, 2006.
- [17] Korgun Koral, Lynn Gargan, Daniel C Bowers, Barjor Gimi, Charles F Timmons, Bradley Weprin, and Nancy K Rollins. Imaging characteristics of atypical teratoid–rhabdoid tumor in children compared with medulloblastoma. *American Journal of Roentgenology*, 190(3):809–814, 2008.
- [18] Jonathan A Forbes, Lola B Chambless, Jason G Smith, Curtis A Wushensky, Richard L Lebow, JoAnn Alvarez, and Matthew M Pearson. Use of t2 signal intensity of cerebellar neoplasms in pediatric patients to guide preoperative staging of the neuraxis. *Journal of Neurosurgery: Pediatrics*, 7(2):165–174, 2011.
- [19] Jonathan A Forbes, Adam S Reig, Jason G Smith, Walter Jermakowicz, Luke Tomycz, Sheila D Shay, David A Sun, Curtis A Wushensky, and Matthew M Pearson. Findings on preoperative brain mri predict histopathology in children with cerebellar neoplasms. *Pediatric neurosurgery*, 47(1):51–59, 2011.
- [20] Andrea Poretti, Avner Meoded, and Thierry AGM Huisman. Neuroimaging of pediatric posterior fossa tumors including review of the literature. *Journal of magnetic resonance imaging*, 35(1):32–47, 2012.
- [21] Darshana D Rasalkar, Winnie Chiu-wing Chu, Bhawan K Paunipagar, Frankie WT Cheng, and CK Li. Paediatric intra-axial posterior fossa tumours: pictorial review. *Postgraduate medical journal*, 89(1047):39–46, 2013.
- [22] Michael J Plaza, Maria J Borja, Nolan Altman, and Gaurav Saigal. Conventional and advanced mri features of pediatric intracranial tumors: posterior fossa and suprasellar tumors. *American Journal of Roentgenology*, 200(5):1115–1124, 2013.
- [23] Luciana Porto, Alina Jurcoane, Dirk Schwabe, and Elke Hattingen. Conventional magnetic resonance imaging in the differentiation between high and low-grade brain tumours in paediatric patients. *European Journal of Paediatric Neurology*, 18(1):25–29, 2014.
- [24] M Koob and N Girard. Cerebral tumors: specific features in children. *Diagnostic and interventional imaging*, 95(10):965–983, 2014.
- [25] Eleni Orphanidou-Vlachou, Nikolaos Vlachos, Nigel P Davies, Theodoros N Arvanitis, Richard G Grundy, and Andrew C Peet. Texture analysis of t1-and t2-weighted mr images and use of probabilistic neural network to discriminate posterior fossa tumours in children. *NMR in Biomedicine*, 27(6):632–639, 2014.
- [26] Yashar Moharamzad, Morteza Sanei Taheri, Farhad Niaghi, and Elham Shobeiri. Brainstem glioma: Prediction of histopathologic grade based on conventional mr imaging. *The neuroradiology journal*, 31(1):10–17, 2018.
- [27] Felice D’Arco, Faraan Khan, Kshitij Mankad, Mario Ganau, Pablo Caro-Dominguez, and Sotirios Bisdas. Differential diagnosis of posterior fossa tumours in children: new insights. *Pediatric Radiology*, 48:1955–1963, 2018.

- [28] Nguyen Minh Duc and Huynh Quang Huy. Magnetic resonance imaging features of common posterior fossa brain tumors in children: a preliminary vietnamese study. *Open Access Macedonian Journal of Medical Sciences*, 7(15):2413, 2019.
- [29] Nguyen Minh Duc, Huynh Quang Huy, Chandran Nadarajan, and Bilgin Keserci. The role of predictive model based on quantitative basic magnetic resonance imaging in differentiating medulloblastoma from ependymoma. *Anticancer Research*, 40(5):2975–2980, 2020.
- [30] Zoran Rumboldt, DLA Camacho, D Lake, CT Welsh, and M Castillo. Apparent diffusion coefficients for differentiation of cerebellar tumors in children. *American Journal of Neuroradiology*, 27(6):1362–1369, 2006.
- [31] Jacob L Jaremko, LBO Jans, Lee T Coleman, and Michael R Ditchfield. Value and limitations of diffusion-weighted imaging in grading and diagnosis of pediatric posterior fossa tumors. *American journal of neuroradiology*, 31(9):1613–1616, 2010.
- [32] Barjor Gimi, Kevin Cederberg, Betul Derinkuyu, Lynn Gargan, Kadriye M Koral, Daniel C Bowers, and Korgun Koral. Utility of apparent diffusion coefficient ratios in distinguishing common pediatric cerebellar tumors. *Academic radiology*, 19(7):794–800, 2012.
- [33] Jonathan G Bull, Dawn E Saunders, and Christopher A Clark. Discrimination of paediatric brain tumours using apparent diffusion coefficient histograms. *European radiology*, 22:447–457, 2012.
- [34] Theodore Pierce, Peter G Kranz, Christopher Roth, Dalun Leong, Peter Wei, and James M Provenzale. Use of apparent diffusion coefficient values for diagnosis of pediatric posterior fossa tumors. *The neuroradiology journal*, 27(2):233–244, 2014.
- [35] Luciana Porto, Alina Jurcoane, Dirk Schwabe, Matthias Kieslich, and Elke Hattingen. Differentiation between high and low grade tumours in paediatric patients by using apparent diffusion coefficients. *European journal of paediatric neurology*, 17(3):302–307, 2013.
- [36] Andrea Poretti, Avner Meoded, Kenneth J Cohen, Michael A Grotzer, Eugen Boltshauser, and Thierry AGM Huisman. Apparent diffusion coefficient of pediatric cerebellar tumors: a biomarker of tumor grade? *Pediatric blood & cancer*, 60(12):2036–2041, 2013.
- [37] D Rodriguez Gutierrez, A Awwad, Lisethe Meijer, M Manita, T Jaspan, Robert A Dineen, Richard G Grundy, and Dorothee P Auer. Metrics and textural features of mri diffusion to improve classification of pediatric posterior fossa tumors. *American Journal of Neuroradiology*, 35(5):1009–1015, 2014.
- [38] Soubhi Zitouni, Gonca Koc, Selim Doganay, Sibel Saracoglu, Kazim Z Gumus, Saliha Ciraci, Abdulhakim Coskun, Ekrem Unal, Huseyin Per, Ali Kurtsoy, et al. Apparent diffusion coefficient in differentiation of pediatric posterior fossa tumors. *Japanese Journal of Radiology*, 35:448–453, 2017.
- [39] Marwa Mohamed Mahmoud Esa, Emad Mohammed Mashaly, Yasser Fouad El-Sawaf, and Mohammed Mahmoud Dawoud. Diagnostic accuracy of apparent diffusion coefficient ratio in distinguishing common pediatric cns posterior fossa tumors. *Egyptian Journal of Radiology and Nuclear Medicine*, 51:1–11, 2020.
- [40] Pham Minh Thong and Nguyen Minh Duc. The role of apparent diffusion coefficient in the differentiation between cerebellar medulloblastoma and brainstem glioma. *Neurology International*, 12(3):34–40, 2020.
- [41] David-Hillel Ruben. *Explaining explanation*. Routledge, 2015.
- [42] Tim Miller. Explanation in artificial intelligence: Insights from the social sciences. *Artificial intelligence*, 267:1–38, 2019.
- [43] David K. Lewis. *Counterfactuals*. Cambridge, MA, USA: Blackwell, 1973.
- [44] Boris Kment. Counterfactuals and explanation. *Mind*, 115(458):261–310, 2006.
- [45] Jim Woodward. Explanation, invariance, and intervention. *Philosophy of Science*, 64(S4):S26–S41, 1997.
- [46] James Woodward, Edward N Zalta, et al. Scientific explanation. *The Stanford*, 2017.
- [47] Edmund L. Gettier. Is justified true belief knowledge? *Analysis*, 23(6):121–123, 1963.

- [48] Christopher Hitchcock. The intransitivity of causation revealed in equations and graphs. *The Journal of Philosophy*, 98(6):273–299, 2001.
- [49] Christopher Hitchcock. Prevention, preemption, and the principle of sufficient reason. *The Philosophical Review*, 116(4):495–532, 2007.
- [50] James Woodward. *Making things happen: A theory of causal explanation*. Oxford university press, 2005.
- [51] Matthew L Ginsberg. Counterfactuals. *Artificial intelligence*, 30(1):35–79, 1986.
- [52] Peter Spirtes, Clark Glymour, and Richard Scheines. Discovery algorithms for causally sufficient structures. *Causation, prediction, and search*, pages 103–162, 1993.
- [53] Peter Spirtes, Clark Glymour, and Richard Scheines. *Causation, prediction, and search*. MIT press, 2000.
- [54] Thomas L Griffiths, Nick Chater, Charles Kemp, Amy Perfors, and Joshua B Tenenbaum. Probabilistic models of cognition: Exploring representations and inductive biases. *Trends in cognitive sciences*, 14(8):357–364, 2010.
- [55] Yu-Liang Chou, Catarina Moreira, Peter Bruza, Chun Ouyang, and Joaquim Jorge. Counterfactuals and causability in explainable artificial intelligence: Theory, algorithms, and applications. *Information Fusion*, 81:59–83, 2022.
- [56] Sahil Verma, Varich Boonsanong, Minh Hoang, Keegan E Hines, John P Dickerson, and Chirag Shah. Counterfactual explanations and algorithmic recourses for machine learning: A review. *arXiv preprint arXiv:2010.10596*, 2020.
- [57] Austin Waters and Risto Miikkulainen. Grade: Machine learning support for graduate admissions. *Ai Magazine*, 35(1):64–64, 2014.
- [58] Monica Andini, Emanuele Ciani, Guido De Blasio, Alessio D’Ignazio, and Viola Salvestrini. Targeting policy-compliers with machine learning: an application to a tax rebate programme in italy. *Bank of Italy Temi di Discussione (Working Paper) No*, 1158, 2017.
- [59] Susan Athey. Beyond prediction: Using big data for policy problems. *Science*, 355(6324):483–485, 2017.
- [60] Jonah E Rockoff, Brian A Jacob, Thomas J Kane, and Douglas O Staiger. Can you recognize an effective teacher when you recruit one? *Education finance and Policy*, 6(1):43–74, 2011.
- [61] Wuyang Dai, Theodora S Brisimi, William G Adams, Theofanie Mela, Venkatesh Saligrama, and Ioannis Ch Paschalidis. Prediction of hospitalization due to heart diseases by supervised learning methods. *International journal of medical informatics*, 84(3):189–197, 2015.
- [62] Katherine Elizabeth Brown, Doug Talbert, and Steve Talbert. The uncertainty of counterfactuals in deep learning. In *The International FLAIRS Conference Proceedings*, volume 34, 2021.
- [63] Ramaravind K Mothilal, Amit Sharma, and Chenhao Tan. Explaining machine learning classifiers through diverse counterfactual explanations. In *Proceedings of the 2020 conference on fairness, accountability, and transparency*, pages 607–617, 2020.
- [64] Seyed-Mohsen Moosavi-Dezfooli, Alhussein Fawzi, and Pascal Frossard. Deepfool: a simple and accurate method to fool deep neural networks. In *Proceedings of the IEEE conference on computer vision and pattern recognition*, pages 2574–2582, 2016.
- [65] Toygar Tanyel, Nadarajan Chandran, Nguyen Minh Duc, and Bilgin Keserci. Deciphering machine learning decisions for distinguishing between posterior fossa tumor types using mri features: What does the data tell us? Available at SSRN 4421493, 2023.
- [66] Nitesh V Chawla and Darcy A Davis. Bringing big data to personalized healthcare: a patient-centered framework. *Journal of general internal medicine*, 28:660–665, 2013.
- [67] Arash Shaban-Nejad, Martin Michalowski, and David L Buckeridge. Health intelligence: how artificial intelligence transforms population and personalized health. *NPJ digital medicine*, 1(1):53, 2018.
- [68] Ketan Paranjape, Michiel Schinkel, and Prabath Nanayakkara. Short keynote paper: Mainstreaming personalized healthcare—transforming healthcare through new era of artificial intelligence. *IEEE journal of biomedical and health informatics*, 24(7):1860–1863, 2020.

- [69] Kevin B Johnson, Wei-Qi Wei, Dilhan Weeraratne, Mark E Frisse, Karl Misulis, Kyu Rhee, Juan Zhao, and Jane L Snowdon. Precision medicine, ai, and the future of personalized health care. *Clinical and translational science*, 14(1):86–93, 2021.
- [70] Sanghamitra Dutta, Jason Long, Saumitra Mishra, Cecilia Tilli, and Daniele Magazzeni. Robust counterfactual explanations for tree-based ensembles. In *International Conference on Machine Learning*, pages 5742–5756. PMLR, 2022.
- [71] Donato Maragno, Jannis Kurtz, Tabea E. Röber, Rob Goedhart, Ş. Ilker Birbil, and Dick den Hertog. Finding regions of counterfactual explanations via robust optimization, 2023.
- [72] Riccardo Guidotti. Counterfactual explanations and how to find them: literature review and benchmarking. *Data Mining and Knowledge Discovery*, pages 1–55, 2022.